

6. Uncertainty in predictions of forest carbon dynamics – separating driver error from model error

Running Title: Partitioning Sources of Model Error

L. Spadavecchia¹, M Williams^{1*}, B Law²

¹ School of GeoSciences, Institute of Atmospheric and Environmental Science,
University of Edinburgh, Edinburgh EH9 3JN, UK.

² Oregon State University,

* Correspondence to Mathew Williams, mat.williams@ed.ac.uk.

KEY WORDS: Spatio-temporal geostatistics, geostatistical simulation, data assimilation, product-sum covariance model, process based modelling, carbon dynamics

* Corresponding Author

6.1 Declaration

The following chapter is intended for submission to *Global Change Biology*. I conducted all the analyses reported, except for the production of the parameter ensemble, which was undertaken by M. Williams using his Ensemble Kalman Filter code. All of the model runs reported were produced using a version of the DALEC model coded by me with reference to M. Williams' original code. I wrote all the body text, except for the sections *Modelling daily exchanges of C and water* (6.4.2) and *DALEC parameterisation* (6.5.1), which were provided by M. Williams. M. Williams also provided comments and made editorial changes to the text.

6.2 Abstract

We present an analysis of the relative magnitude and contribution of parameter and driver uncertainty to the uncertainty of estimates of net carbon fluxes. Model parameters may be difficult or impractical to measure, whilst driver fields are rarely complete, with data gaps due to sensor failure. Parameters are generally derived through some optimisation method, whilst driver fields may be interpolated from available data sources. For this study, we used data from a young Ponderosa pine stand at Metolius, Central Oregon, and a simple model of coupled carbon and water fluxes (DALEC). We retrieved a set of 375 acceptable parameterisations *via* an Ensemble Kalman filter, which used observations of net C exchange to retrieve model parameters. We generated an ensemble of meteorological driving variables for the site, consistent with the spatio-temporal autocorrelations inherent in the observational data *via* geostatistical simulation. The simulated meteorological dataset was propagated through the model to derive the uncertainty on the CO₂ flux resultant from driver uncertainty typical of spatially extensive modelling studies. Furthermore, we partitioned the model uncertainty between temperature and precipitation, to examine which driver contributes the most to the net flux uncertainty. Our results indicated that driver uncertainty was relatively small (~10 % of the total net flux), whilst parameterisation uncertainty was larger, ~50 % of the total net flux. The largest source of driver uncertainty was due to temperature (8% of the total flux). The combined effect of parameter and driver uncertainty was ~53 % of the total net flux. We discuss issues of bias in contributing to flux errors, and identified bias problems with both temperature and precipitation data. We recommend better constraint of temperature fields when attempting regional to catchment scale modelling,

but suggest that parameterisation issues are of greater importance to constrain the CO₂ flux, presenting novel challenges for regionalised modelling of C dynamics.

6.3 Introduction

Modern catchment scale studies of environmental phenomena commonly employ some sort of modelling approach for extrapolation and prediction (Law et al., 2001a; Running, 1994; Runyon et al., 1994; Williams et al., 2001b; Williams et al., 2005b). In general, the practitioner is faced with the problem of upscaling detailed observations made at a small number of sites to a wider area, due to the expense and technical difficulties associated with direct observation (Thornton et al., 1997; Williams et al., 2005b). Process based models formalise knowledge of ecological processes, and allow integration of observations at various scales to be incorporated into regional analyses (Canham et al., 2003; Heuvelink and Webster, 2001; Williams et al., 2005b). Such models typically require initial estimates of rate parameters and surface characteristics, along with a set of meteorological driving variables, from which estimates of the state vector are derived.

The situation is complicated by the difficulty in measuring and setting parameters, and finding adequate data to drive the model. On one hand, parameters may be difficult or impossible to measure in practice, particularly if the rates of the processes they represent are slow, with time constants greater than a few months. On the other hand, sourcing adequate data to drive the model over the required spatio-temporal extent may be difficult due to sparse sensor networks and missing observations resultant from sensor failure etc. (Thornton et al., 1997).

Partitioning Sources of Model Error

In general we rely on some optimisation procedure to infer appropriate parameter sets (e.g. Klemedtsson et al., 2007; Williams et al., 2005b), and utilise interpolation schemes to gap-fill meteorological drivers (e.g. Daly et al., 1994; Goovaerts, 2000; Hudson and Wackernagel, 1994; Hungerford et al., 1989; Running et al., 1987; Thiessen, 1911; Thornton et al., 1997). The errors resultant from these activities are difficult to quantify, and in the case of driver interpolation rarely explored (Fuentes et al., 2006).

Parameter errors can be explored through a variety of techniques, usually based on Monte Carlo analyses: Parameters may be perturbed by a series of fixed percentages to probe the effect on the state vector (e.g. Oijen et al., 2005; Williams et al., 2005b). More formally, we may chose to parameterise the model using a Bayesian framework, and directly sample parameter error from the posterior distribution of the parameter set computationally (Kennedy et al., 2008; Klemedtsson et al., 2007; Verbeeck et al., 2006). Here we explore an alternative Bayesian technique, whereby an *a priori* parameter set is updated by comparing the model trajectory with observations via data assimilation. This technique has been popular amongst meteorologists and oceanographers (Eknes and Evensen, 2002; Evensen, 1994), and confers the advantage of balancing the observation and model error in an optimal sense (Maybeck, 1979).

Quantification of error resultant from meteorological driver uncertainty may be assessed through geostatistical simulation techniques (Fuentes et al., 2006; Goovaerts, 2001). We generate a moderately large ($n \sim 1000$) ensemble of equi-probable meteorological fields from the available observations, honouring the spatio-temporal autocorrelation structure of the data. The error magnitude of the state vector is quantified after propagating the ensemble through the model *via* Monte Carlo analysis of the n model estimates (e.g. Fuentes et al., 2006).

Partitioning Sources of Model Error

In a previous paper we illustrated the issue of driver error inflation with data scarcity when utilizing geostatistical upscaling of meteorological drivers over a moderately large spatio-temporal extent (Spadavecchia and Williams, In review). However, it is not clear how errors in the meteorological fields affect the state vector, especially in the light of error reduction over increasing temporal support (Spadavecchia and Williams, In review): Processes which respond instantaneously to the driver fields are likely to have larger error magnitudes than those which integrate driving variables over time. As a result, driver errors, which in some cases are appreciable (Spadavecchia and Williams, In review), may in fact cancel out over the model run.

We present an analysis of the sources and magnitude of model errors using DALEC; a simple process-based ecosystem model of coupled carbon and water dynamics. The model is multi-output, supplying estimates of C stocks, soil moisture and fluxes of carbon and water on a daily time-step. We parameterise the model for a well-sampled Ponderosa pine forest at Metolius, Central Oregon *via* the Ensemble Kalman filter (EnKF) (Evensen, 2003), and sample the uncertainty in the net ecosystem carbon exchange (NEE) associated with parameter uncertainty. We then replace the observed meteorology with an ensemble of geostatistical simulations conditioned on observations surrounding the study site, and run the parameterised model to sample the resultant uncertainty in NEE due to driver uncertainty. Finally, we undertake a full uncertainty analysis *via* Monte Carlo sampling of both parameter and driver sets to examine the cumulative uncertainty of the NEE.

The objectives of this paper are to examine and compare the magnitude of model error resultant from parameter uncertainty and driver uncertainty on a fine temporal support of one day. Furthermore, we intend to characterise the error magnitude resultant from uncertainty in a variety of daily driver fields, to diagnose

Partitioning Sources of Model Error

which fields are critical to constrain model predictions. In doing so we aim to address the following hypotheses:

- **H1:** Driver error will be larger than the parameter error, since the likely range of parameters are well constrained locally, whilst meteorological simulations are conditioned on patchy, spatially dispersed data.
- **H2a:** Precipitation will contribute most to model uncertainty: Precipitation has the largest interpolation error, and ecosystem production is drought-limited in the study region (Law et al., 2001a; Van Tuyl et al., 2005).
- **H2b:** Temperature will contribute most to model uncertainty: Errors associated with precipitation will average out over time, as plant response to precipitation is resultant from drought. Drought integrates precipitation uncertainty over time through soil moisture content, so instantaneous temperature effects on heterotrophic processes will dominate the NEE error signal.

6.4 Methods

6.4.1 Study Site

The Metolius young Ponderosa Pine site is located on a private forestry concession near the Metolius Natural Research area (44°26'N, 121°34'W, elevation ~ 1165m) (Figure 6.1). The site was clear-cut in the late 1980s, and since then has been allowed to naturally regenerate, with some thinning in 2002. The canopy layer is exclusively comprised of *Pinus ponderosa*, with an understory of *Purshia tridentata* and *Pteridium aquilinum*, and a herb layer of *Fragaria vesca*. From 2000-2002 the site had a continuously functioning eddy covariance system, forming part of the Ameriflux observational network. Fluxes were measured at ~9m above the canopy. The site is

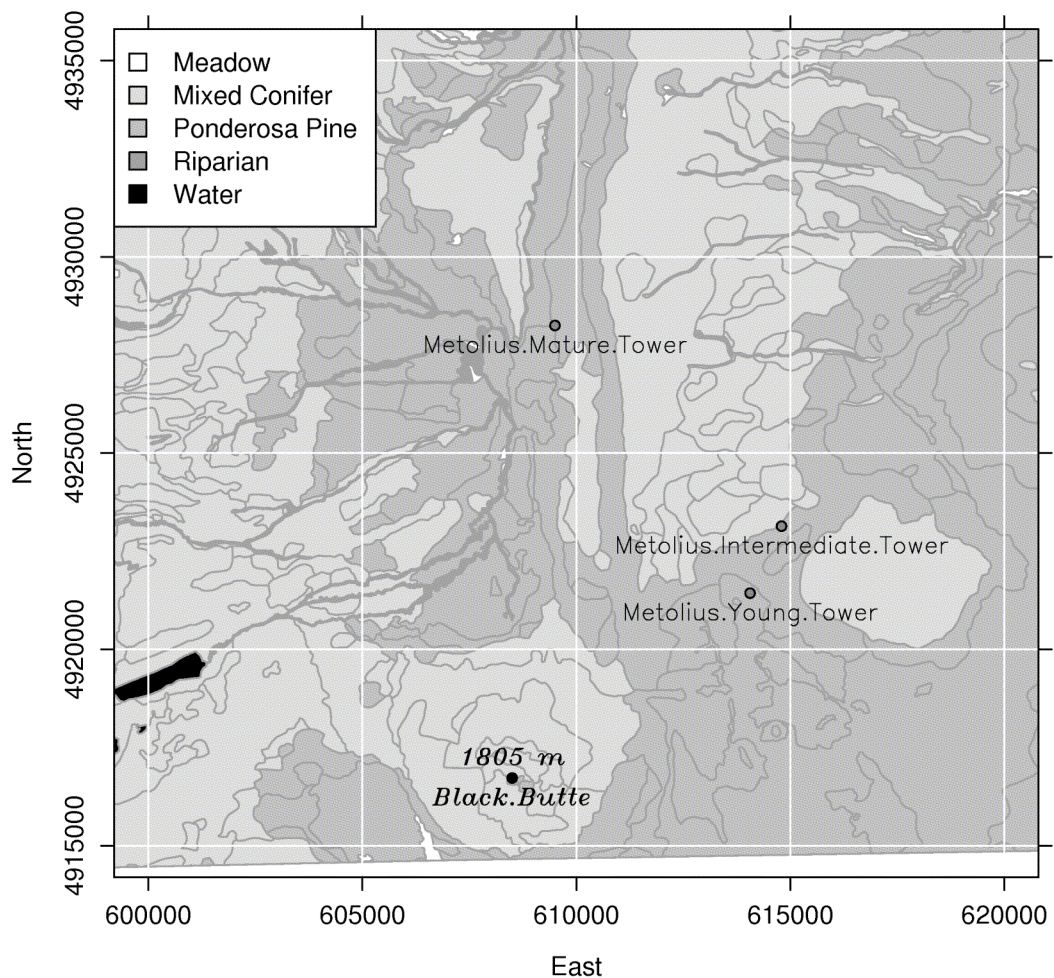


Figure 6.1 Metolius Young Ponderosa pine site and surrounding area, Deschutes County, Oregon. Two other Ameriflux towers are situated to the north. The area is extensively forested with Ponderosa pine and mixed coniferous vegetation (vegetation data courtesy of USDA forest service: Sisters Ranger Station, Sisters, Oregon).

characterised by warm dry summers and wet cool winters. Diurnal temperature variation can be high (1.5 – 18.6 °C), and the site is prone to drought (mean annual precipitation = 402 mm, mean number of dry days = 224). Two other flux towers are positioned to the north of the site, one of which (Metolius intermediate Ponderosa Pine site) has been in continuous operation since 2002. No flux data from these towers is employed in this study, although Meteorological observations from the intermediate tower are used: The locations are indicated primarily to provide context with earlier studies.

6.4.2 Modelling daily exchanges of C and water

6.4.2.i Canopy processes

The model consists of a 'big leaf' photosynthesis (GPP) and evapotranspiration (ET) model (Aggregated Canopy Model, ACM: Williams et al., 1997) coupled to a module that tracks the allocation and mineralisation of carbon, and a module that tracks the dynamics of soil moisture. This coupled model is henceforth referred to as the data assimilation linked ecosystem carbon model, or DALEC model (Figure 6.2).

The ACM calculates GPP and ET as a function of vegetation properties (leaf area index, and foliar N for GPP), meteorology (maximum daily temperature, daily temperature range, maximum daily vapour pressure deficit, total daily irradiance) and soil properties (soil hydraulic resistance and soil water potential). The ACM model was parameterised from locally calibrated SPA predictions of GPP and ET (Schwarz et al 2004), using the approach laid out in Williams et al. (1997).

6.4.2.ii C cycling

The carbon module apportions the predicted gross primary production (GPP) into autotrophic respiration and the growth of plant C pools (DALEC: Williams et al., 2005b) and then tracks additions to and mineralisation of litter and soil organic matter (SOM). DALEC requires the specification of ten carbon parameters to control the fate of C in the ecosystem. These parameters relate to the rate of decomposition, fraction of GPP respired, fraction of NPP allocated to foliage, fraction of remaining NPP allocated

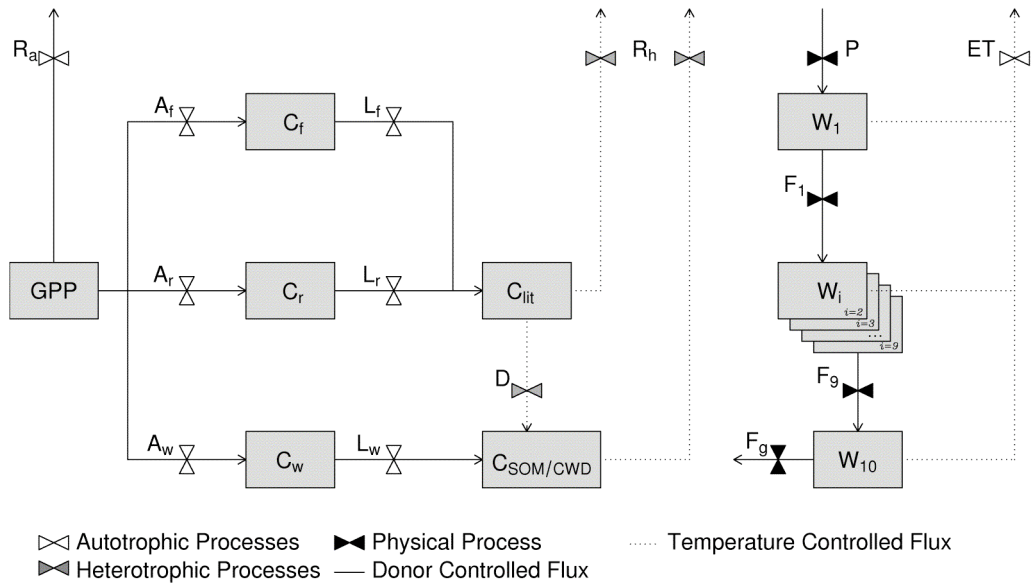


Figure 6.2 DALEC C and Water dynamics model. Pools are shown as grey boxes, whilst fluxes are represented as arrows. The left hand plot illustrates the C module: GPP (gross primary production) is allocated to foliage (f), roots (r) or woody (w) material. Allocation fluxes are marked A, whilst losses are marked L. C loss is through respiration fluxes (R), split between autotrophic (a) and heterotrophic (h) sources. The right panel details the flow of water through the model: Precipitation (P) is allocated between 10 soil water layers ($W_{1...10}$). Vertical drainage flows ($F_{1...9}$) occur when soil layers are saturated. Water may be lost through gravitational drainage (F_g) to groundwater or evapotranspiration (ET).

to fine roots, turnover rates of foliage, wood, fine roots, litter and SOM, and the temperature sensitivity of litter and SOM mineralisation. DALEC also requires an initial estimate of the C stock present in five pools; foliage, fine roots, woody stems, litter and SOM (see Williams et al., 2005b).

The model takes daily inputs of minimum temperature (T_{min}), maximum temperature (T_{max}), and precipitation (P). Temperature observations are converted to daily average temperature (T_a), maximum daily vapour pressure deficit (VPD), and solar radiation (RAD) using well-tested relationships (Running et al., 1987; Thornton et al., 1997). VPD is estimated using Murray's formula (Murray, 1967), whilst RAD is predicted using the Allen model (Allen, 1997). Details of these models are provided in the appendix.

6.4.2.iii Modelling soil water dynamics and drought stress

Based on intensive hourly modelling studies at the site (Williams et al. 2001, Schwarz et al 2004), we generated a simple daily model of soil water dynamics. The model tracks water inputs and outputs in a 10 layer 'bucket' model extending to 3 m in depth. Moisture is drained from soil layers when water content exceeds field capacity. We used relationships from Saxton et al (1986) and local measurements of soil texture to determine porosity and field capacity. Soil hydraulic resistance was determined based on soil texture, root biomass and water fraction in each soil layer (Williams et al 2001). Soil water potential (Ψ_s) was generated from a locally determined empirical relationship ($\Psi_s = -1.74 + 3.997\theta$) on soil water fraction (θ). Rooting depth was determined as a function of root biomass using data from nearby ponderosa pine stands (Schwarz et al 2004). More details of this approach are provided in Fisher et al. (In press).

6.4.3 Data

6.4.3.i Flux Observations

We used three years of data from the Metolius young Ponderosa pine plot (Law et al., 2001a; Law et al., 2001b) to parameterise DALEC. The data consist of records of net ecosystem exchange (NEE), total ecosystem respiration (Re), evapotranspiration (ET) and a set of meteorological observations, sampled at the daily time-step. Direct observation of T_{min} , T_{max} , T_a , P , VPD and RAD were made simultaneously with the flux data.

There were 684 daily NEE observations over the 1096 days from 2000-2. Gaps in the data resulted from sensor failure and filtering to remove observations with low friction velocity (u^*), or physically implausible magnitudes ($|F_c| > 25 \mu\text{mol m}^{-2} \text{sec}^{-1}$).

6.4.3.ii Canopy Density Observations

In order to constrain the parameterisation of DALEC, we utilised observations of the leaf area index (LAI) of the forest canopy. Observations were made at four times during the three-year period, using an LAI-2000 plant canopy analyser (LI-COR, Lincoln, NE, USA). Observations were collected on a 10 m square grid, and were corrected for clumping at the needle, shoot and stand levels (Law et al., 2001c; Law et al., 2001d). These observations were related to the model foliar carbon estimate *via* direct measurements of the specific leaf mass from foliage samples, see Williams (2005) for further details.

We augmented this set of observations with retrievals of LAI from the MODIS satellite (Knyazikhin et al., 1998; Myneni et al., 2002), with a sampling frequency of eight days. We filtered the MODIS LAI observations using the provided QC flags, to reject data from cloudy days or aberrant spectral signatures (Knyazikhin et al., 1998).

6.4.3.iii Meteorological Observations

In order to generate meteorological simulations at the study site, we sourced the 13 closest meteorological monitoring stations with data available for the period 2000-2002 (Table 6.1, Figure 6.3). These stations were selected so that there would be a minimum of 8 T_{min} , T_{max} , and P observations per day on which to condition meteorological simulations. Observations were filtered such that the values would not exceed the state extremes for Oregon (National Oceanic and Atmospheric Administration (NOAA), Silver Spring, Maryland, USA). Meteorological records for stations further than 25km away were also sourced to examine the effect of data scarcity on NEE uncertainty Figure 6.3.

Table 6.1 Locations and data summary for surrounding meteorological stations

Name	East*	North*	Elevation*	Network	Records Began	Distance to Site [†]	T _{min} °C	T _{max} °C	Precip. mm [‡]
<i>Belhap Springs</i>	577110	4905648	677	COOP	1960	40	2.8 (4.8)	16.3 (10.5)	6.7 (15.2)
<i>Marion Forks Hatchery</i>	583329	4939053	804	COOP	1948	35	2.0 (4.6)	15.1 (9.8)	4.3 (8.8)
<i>Redmond FAA Airport</i>	647656	4903155	935	COOP	1948	38	0.3 (6.2)	17.5 (9.7)	0.7 (2.2)
<i>Santiam Junction</i>	582241	4920523	1121	COOP	1986	32	-1.0 (5.1)	13.0 (10.1)	5.3 (11.5)
<i>Sisters</i>	615665	4906216	966	COOP	1958	15	-0.3 (5.9)	16.1 (10.5)	0.8 (3.0)
<i>Colgate</i>	610384	4907884	1010	RAWS	1985	14	0.1 (5.6)	17.8 (10.2)	0.9 (3.5)
<i>Haystack</i>	649826	4923610	985	RAWS	1985	36	3.9 (6.5)	16.0 (9.9)	0.4 (2.2)
<i>Metolius Arm</i>	610194	4942510	1029	RAWS	1991	21	3.4 (6.2)	15.5 (10.3)	1.4 (5.0)
<i>Pebble</i>	580919	4898658	1076	RAWS	1991	40	2.9 (5.3)	15.4 (9.1)	3.4 (7.9)
<i>Marion Forks</i>	582030	4937184	1111	SNOTEL	1981	36	2.4 (4.6)	14.0 (10.5)	4.4 (9.7)
<i>Santiam Junction</i>	584894	4920557	1165	SNOTEL	1979	29	0.0 (5.1)	13.6 (9.4)	4.4 (9.2)
<i>Hogg Pass</i>	590225	4918777	1439	SNOTEL	1980	24	0.5 (5.8)	11.5 (9.6)	5.1 (9.8)
<i>Otter Intermediate Tower</i>	614792	4923138	1253	AMERIFLUX	2001	2	4.1 (7.1)	12.4 (8.9)	0.5 (1.9)

Mean meteorological observations. Standard deviations indicated in parentheses.

* Coordinates in meters UTM zone 10, WGS84 datum.

[†] Distance to Metolius Young Ponderosa pine site (km).

[‡] Daily mean precipitation (mm); insufficient data at some sites for reliable annual averages.

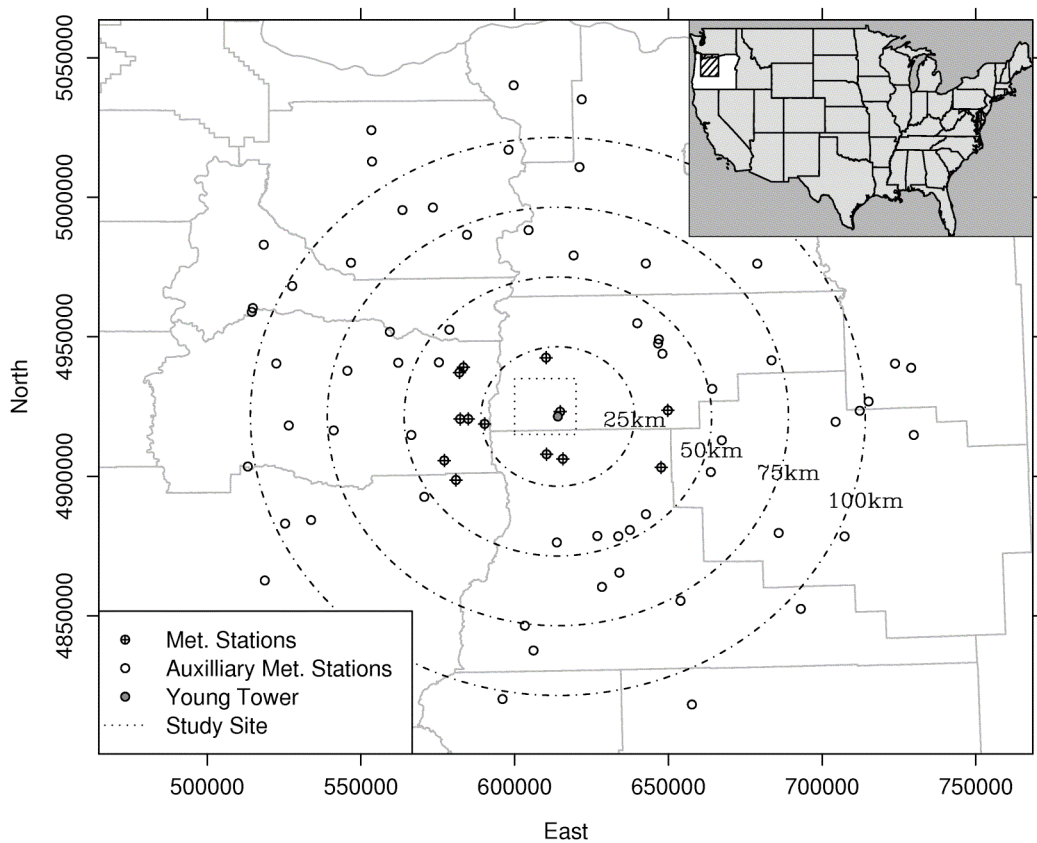


Figure 6.3 Meteorological monitoring stations surrounding the Metolius Young Ponderosa pine site, indicated as a gray point. Crosshairs represent the 13 core stations used for the simulations, whilst auxiliary stations at increasing distance from the study site are indicated as open circles. Light grey lines indicate county boundaries. The extent of figure 6.1 is indicated as a broken black rectangle, which lies in Deschutes County.

6.4.4 DALEC Parameterisation

Many of the parameters associated with the processes of photosynthesis, evapotranspiration and soil water physics have been derived from the literature or from previous research at the study site (Schwarz et al., 2004; Williams et al., 2001a; Williams et al., 2005a). The most uncertain parameters are the 10 associated with respiration, turnover and allocation of C among plant and soil pools. We add an eleventh parameter

Partitioning Sources of Model Error

to these, the parameter from the ACM GPP model that relates foliar N content to photosynthetic capability, to include an estimate of uncertainty in the GPP calculations.

We used an Ensemble Kalman filter (EnKF, Williams et al 2005) to estimate the likely distributions for these uncertain parameters. The EnKF combines a model of a system (i.e. DALEC) with observations of that system over time (i.e. NEE and LAI observations). The model generates predictions of the state vector (C pools and fluxes, soil moisture and water fluxes) for each time step. NEE and LAI predictions are then compared with independent observations. Based on an assessment of model forecast and observational uncertainty, the predicted NEE and LAI are adjusted. The model error covariance matrix, as determined in the EnKF, is then used to adjust the full state vector accordingly.

We adjusted the EnKF approach used in Williams et al. (2005) from a state estimation problem to a parameter estimation problem. We added the 11 model parameters to the state vector supplied to the EnKF. We set the model error on the fluxes and pools of C and water to relatively low values (0.01%) compared to the uncertainty on the 11 parameters (0.2%). The error on the NEE observations was estimated at $0.7 \text{ gC m}^{-2} \text{ d}^{-1}$ and on LAI estimates at 10%. The number of ensembles used was set at 400.

The initial EnKF analysis used parameter estimates from an earlier study (Williams et al. 2005). After the initial analysis, we used the final parameter estimates to reinitialise the parameters, and ran the EnKF again. We repeated this process again, at which point the parameter ensembles stabilised.

We then ran the model with each element of the acceptable parameter ensemble in turn to evaluate the effect of parameter uncertainty on the NEE estimate (experiment 1).

6.4.5 Meteorological Simulation

In order to quantify the uncertainty of interpolated driving variables at the Metolius site, we employed the sequential Gaussian simulation (SGS) (Goovaerts, 1997), which may be regarded as an extension of the commonly used Kriging technique (e.g. Ashraf et al., 1997; Goovaerts, 2000; Hudson and Wackernagel, 1994; Spadavecchia and Williams, In review).

Kriging estimates represent the most likely value of the estimate given the surrounding observations, based on a probabilistic model. Kriging variances produce a valid estimate of uncertainty for the estimate when taken in isolation, but they are less useful for assessing the uncertainty of the regionalisation as a whole (Goovaerts, 1997). SGS expands on Kriging by drawing equally possible realisations of the whole field from the probabilistic model, preserving the surface roughness of the estimated field and avoiding the characteristic smoothing effect of Kriging (Deutsch and Journel, 1998; Goovaerts, 1997; Goovaerts, 1999; Goovaerts, 2001). The outcome is a set of equally likely estimates of the meteorology at the study site given our limited knowledge.

We modelled the autocorrelation structure of the T_{min} , T_{max} and P observations at the meteorological stations by calculating their empirical semivariograms. The semivariogram γ quantifies the dissimilarity between pairs of observations separated by increasing spatiotemporal lag distances:

$$\gamma(h_u, h_t) = \frac{1}{2N(h_u, h_t)} \sum_{i=1}^{N(h_u, h_t)} [z(u_i, t_i) - z(u_i + h_u, t_i + h_t)]^2 \quad (6.1)$$

Where h_u and h_t are the separation lags in space and time respectively, $z(u, t)$ is the observed variable at a given spatio-temporal coordinate, $N(h_u, h_t)$ is the number of pairs in the lag.

Partitioning Sources of Model Error

We selected and fit permissible semivariance models (Christakos, 1984; Gringarten and Deutsch, 2001; Mcbratney and Webster, 1986) to summarise the empirical semivariograms. The spatial and temporal semivariogram models were then combined using the product-sum covariance model of De Cesare et al. (De Cesare et al., 2001; De Iaco et al., 2001).

Simulation proceeded as follows:

1. Initialise a random visiting schedule for the grid of G locations, with a data heap of n observations.
2. Visit the i^{th} node of the grid and estimate the mean and variance *via* Kriging conditioned on the values in the data heap.
3. Draw a random value from the Gaussian distribution of the node, defined by the Kriging estimate (mean) and Kriging variance. The resultant value was the SGS estimate \tilde{z}_i^* .
4. The realization \tilde{z}_i^* was then treated as an observation for subsequent estimates, and added to the data heap ($n+i$ conditioning data).
5. Iterate from 2 until all grid locations were visited ($i=G$).

As in all geostatistical techniques, it is possible to incorporate covariates into the simulations: We specified a linear lapse relationship between elevation and temperature, and a longitudinal gradient in precipitation, the parameters of which were estimated as part of the simulation process, via the external drift method (Hudson and Wackernagel, 1994; Wackernagel, 1998).

6.4.6 Partitioning Driver Uncertainty

We generated 1000 simulations of T_{min} , T_{max} and P at the Metolius site for the full three years of the study conditioned on data from the 8 closest spatial neighbours over a temporal window of ± 10 days (88 observations) *via* SGS. Meteorological observations at the site were excluded so as to explore the uncertainty resultant from modelling C dynamics over sparsely sampled regions. We then ran the parameterised model with each of the 1000 simulations in turn, to inspect the variability in the predicted NEE ensemble. We then ran three experiments; (2.i) locally observed temperatures, VPD and RAD with simulated precipitation, (2.ii) locally observed precipitation with simulated temperatures, VPD and RAD (2.iii) locally observed precipitation, VPD and RAD with simulated temperatures. Experiment 2.iii was devised to decouple the NEE uncertainty resultant from deriving VPD and RAD from temperature within the model. Finally, having generated a parameter ensemble and 1000 equi-probable meteorologies, we generated a sample of 1000 parameter and meteorology permutations to test the combined effect of parameter and driver uncertainty on the model (experiment 3).

In order to test H2 we compared the precipitation regime of the data with the simulated rainfall trajectories. We calculated the number of days since a precipitation event ($n_{p=0}$) for the 1000 simulations generated in experiment 2.i. We subtracted the number of days since a precipitation event in the local observations from $n_{p=0}$ to generate a metric of drought (Δ_p). We considered data where Δ_p was positive (i.e. simulations with longer dry spells than observed in the data) to examine the effect of drought on the uncertainty of the NEE trajectory.

Partitioning Sources of Model Error

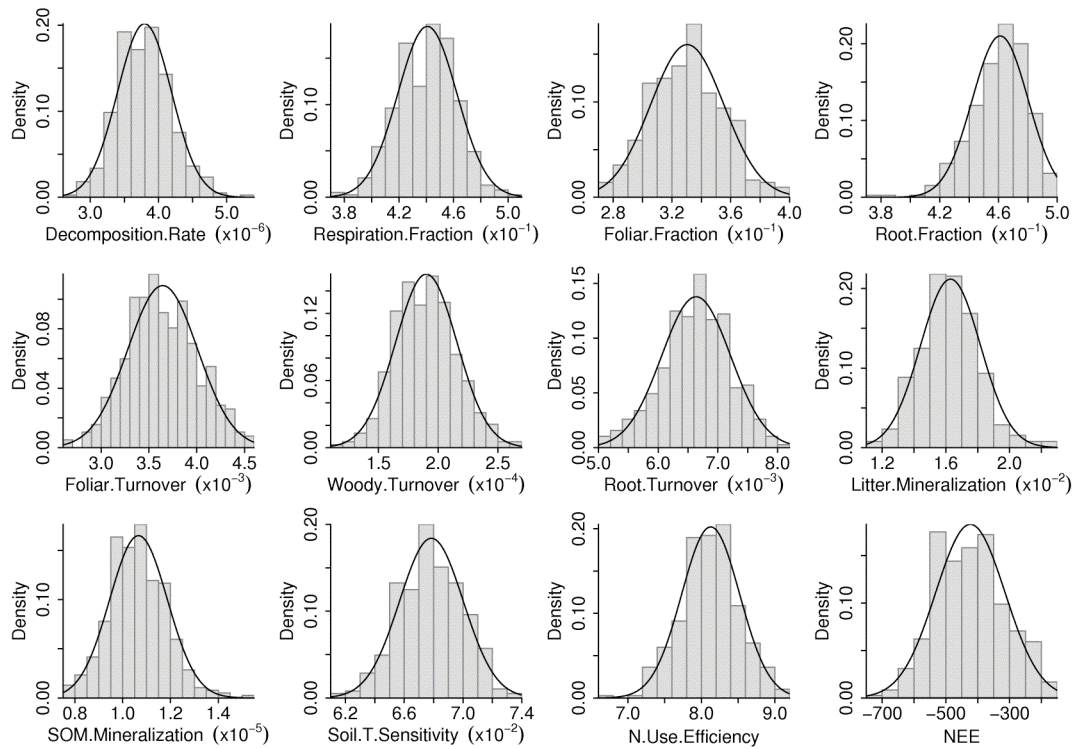


Figure 6.4 Marginal parameter distributions retrieved from an ensemble of 375 elements derived from the Ensemble Kalman filter and passing a goodness-of-fit test against the observed NEE time series 2000-2002. The resultant total net ecosystem exchange (NEE gC m^{-2}) over three years is also indicated.

6.4.7 Sparsity of Meteorological Conditioning Data

Given that interpolation uncertainty is related to the distance to the nearest neighbours (Spadavecchia and Williams, In review), we investigated the effect of increasing data sparsity by conditioning simulations on data from increasing search radii (Figure 6.3), ignoring weather stations closer than the threshold distances of 25, 50, 75 and 100 km. In each case, the closest 4 stations beyond the threshold distance were used to condition the simulations. We ran the model with each of these meteorological ensembles to test the robustness of the comparison of meteorological and parameterisation uncertainties on the uncertainty of the final NEE analysis (experiment 4).

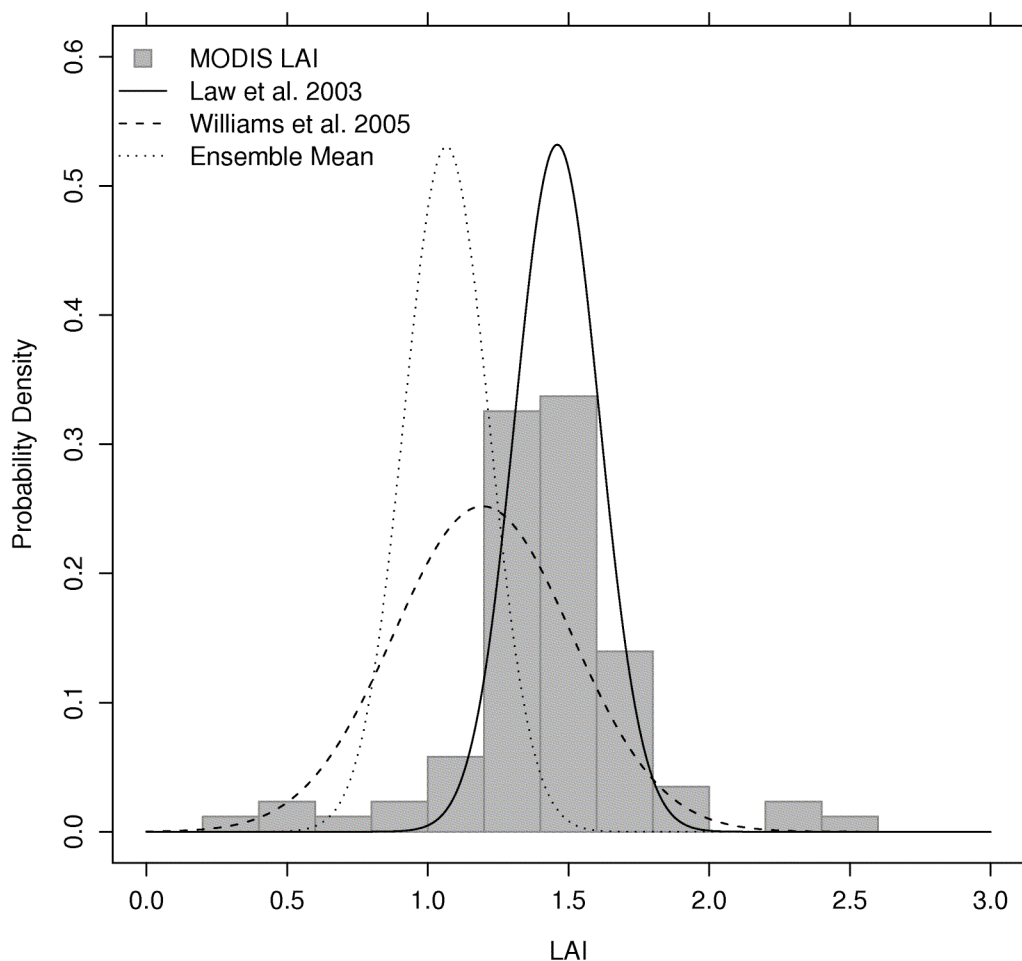


Figure 6.5 MODIS leaf area index (LAI) distribution for the Metolius Young Ponderosa pine site for a three-year period (2000-2002). Reported distributions from the literature are also indicated as solid and broken black lines. The finely broken black line indicates the 375-element ensemble mean retrieved from the Ensemble Kalman Filter.

6.5 Results

6.5.1 DALEC Parameterisation

The EnKF propagated observations of NEE and LAI into an ensemble of 400 state vector predictions, thereby generating estimates of the 11 parameters included in the state vector. These ensembles were subject to a Chi-Squared goodness of fit test of the NEE observations as a check on the parameterisations. The DALEC model was

Partitioning Sources of Model Error

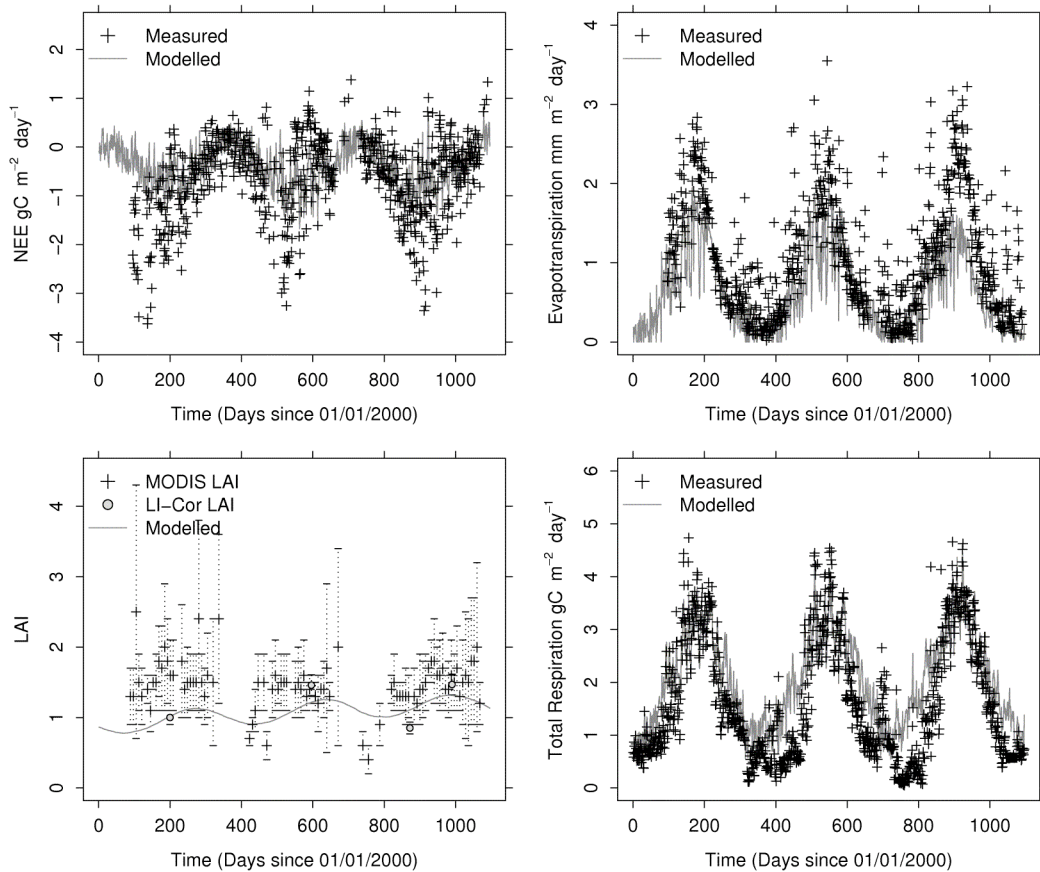


Figure 6.6 Model data comparison for four fluxes. In all cases the dark grey line indicates the mean trajectory of the 375-element ensemble trajectory retrieved from the Ensemble Kalman filter. Observations are indicated as black crosses. The modelled LAI is compared with ground based Li-Cor LAI2000 observations and MODIS satellite retrievals. LAI error bars are included to show the high variability of the satellite retrievals.

run in normal forward mode (i.e. without the EnKF) using each of the 400 sets of parameter estimates, and the chi-squared test was applied on the predictions and observations of daily NEE to test their similarity. Of the 400 parameter sets, 375 passed this test ($\chi^2 = 717$, $DF = 656$, $P > 0.95$) and were used in further analyses. The distribution of the parameter ensembles is illustrated in Figure 6.4, along with the resultant total NEE distribution.

The model ensemble appeared to represent the LAI reasonably well, and seemed to be in good agreement with the various available data sources for the site (Figure 6.5). A t-test indicated no significant difference between the means of the LAI2000 and

Table 6.2 Summary of model fits for various model outputs

Data Source	r^2	RMSE	Pearsons r	kendalls τ
<i>NEE</i> [*]	0.39	8.70	0.62	0.44
<i>ET</i> [†]	0.55	9.90	0.74	0.55
<i>Li-Cor LAI2000</i> [‡]	0.70	0.12	0.84	0.67
<i>MODIS LAI</i> [‡]	0.03	1.34	0.17	0.15
<i>R_e</i> [§]	0.78	13.00	0.88	0.67

* Net ecosystem exchange, $\text{gC m}^{-2} \text{ day}^{-1}$

† Evapotranspiration, $\text{mm m}^{-2} \text{ day}^{-1}$

‡ Leaf Area Index, unitless

§ Total ecosystem respiration, $\text{gC m}^{-2} \text{ day}^{-1}$

MODIS distributions ($t = -1.7$, $P = 0.09$), although this is may have been due to the large uncertainties attached to the MODIS retrievals. Despite the good match between MODIS LAI and the ground observations, the model LAI was found to be significantly different ($t = -142.9$, $P < 0.001$); the mean MODIS LAI was 1.5, significantly higher than the mean model LAI of 1.1.

Visually examining the mean ensemble trajectory for four major components of the flux indicated that NEE and LAI were well reproduced, while the trajectories of total ecosystem respiration (R_e) and evapotranspiration (ET), data not used in the assimilation, were reasonably replicated (Figure 6.6). Quantitative tests revealed the model to be performing well with respect to all data streams, except the MODIS LAI, which appeared to be an overestimate with respect to the model trajectory (Table 6.2).

The optimised model estimated a total carbon uptake of 423 gC m^{-2} over three years, with a 95% confidence interval of $\pm 213.64 \text{ gC}$. The NEE uncertainty resultant from parameterisation was therefore substantial, representing 51% of the total net flux. A detailed analysis of the NEE error indicated relatively unbiased estimates; a simple linear regression between the estimates and observations indicated an intercept of -0.299 and a slope of 0.302 (Figure 6.7), suggesting that the model tended to smooth the NEE

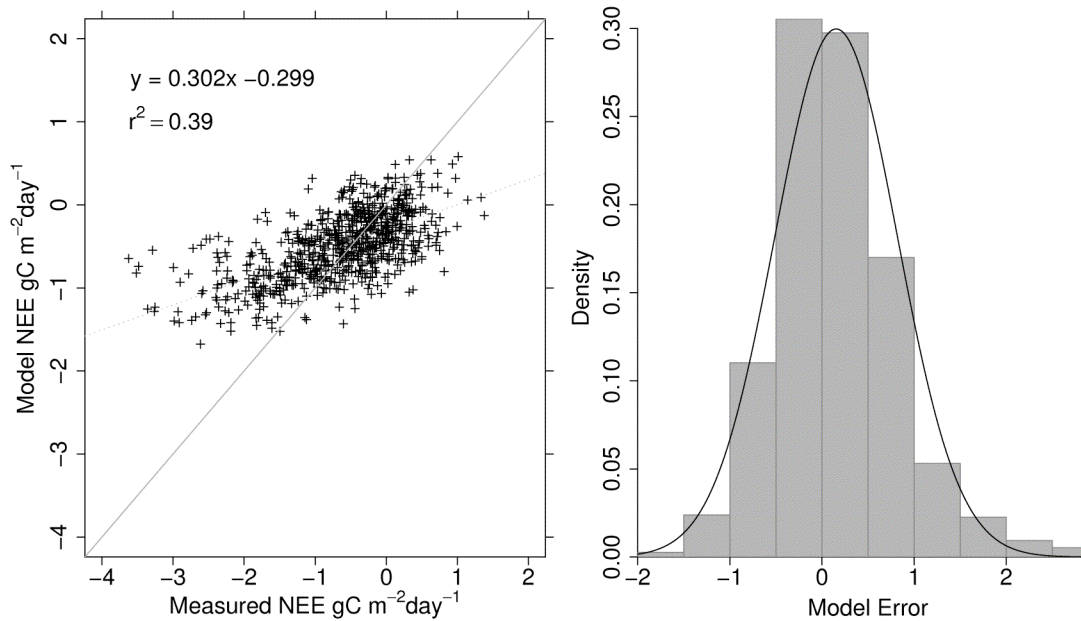


Figure 6.7 Net ecosystem exchange (NEE) model data comparison. Model values are the 375-element ensemble means retrieved from the Ensemble Kalman filter. The model error distribution is indicated in the right panel. The heavy right hand tail indicates an underestimate of the summer C uptake.

trajectory, underestimating the distribution at the extremes, with a small bias towards underestimation of the daily C uptake.

6.5.2 Meteorological Simulation

In order to simulate an ensemble of meteorological regimes we first calculated semivariograms for T_{min} , T_{max} and P . We modelled the spatial variation of T_{min} and T_{max} with a nested spherical ($\varphi_{u,spb} T_{min} = 23.8$ km, $\varphi_{u,spb} T_{max} = 9.67$ km), exponential model ($\varphi_{u,exp} T_{min} = 154.2$ km, $\varphi_{u,exp} T_{max} = 196.6$ km). For P , a Gaussian model ($\varphi_{u,gaus} = 34.7$ km) with a small nugget effect ($\tau = 0.2$ mm) best captured the patterns of spatial variation. All three variables displayed exponential semivariance structures in time, with ranges of ~ 1 week for T_{min} and T_{max} , and a shorter temporal range of 2 days for precipitation, indicating lower temporal continuity in the time series. The sill parameters fitted for each variable were $sill_u = 6.4$, $sill_t = 11.69$ and $sill_g = 12.8$ for T_{min} ; $sill_u = 10$, $sill_t = 23.1$

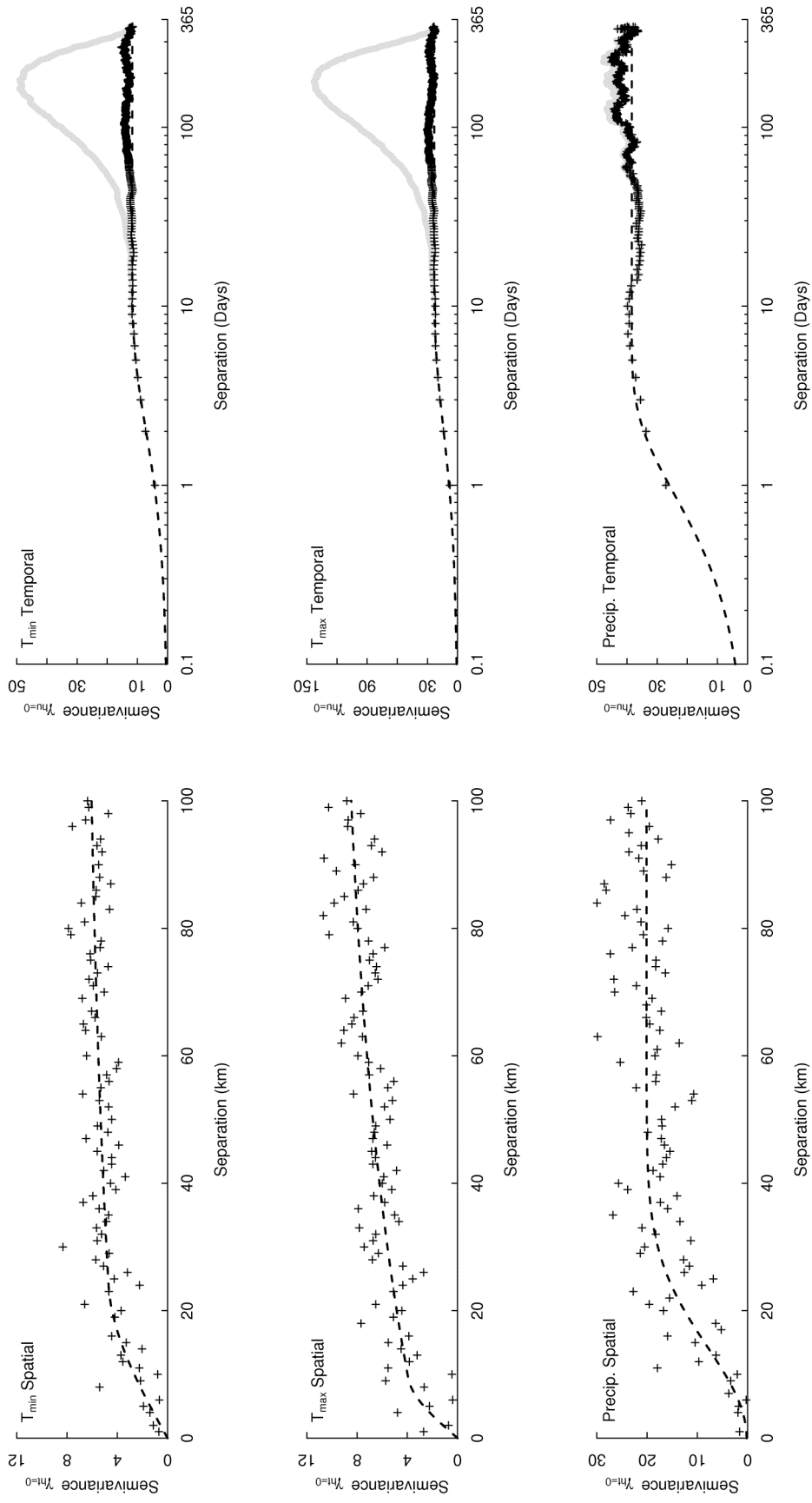


Figure 6.8 Semivariograms of meteorological data from the Central Cascades study area. Data were de-trended prior to analysis. Spatial semivariograms ($\gamma_{h=0}$) were constructed by considering pairs of observations from the same day at increasing spatial separations. Temporal semivariograms ($\gamma_{h=0}$) were constructed from pairs of observations from the same station at increasing temporal separation, and plotted on a log axis for clarity. For all plots, detrended observations are shown as black crosses and semivariogram models are indicated as broken black lines. Grey points on the temporal plots are raw data prior to detrending.

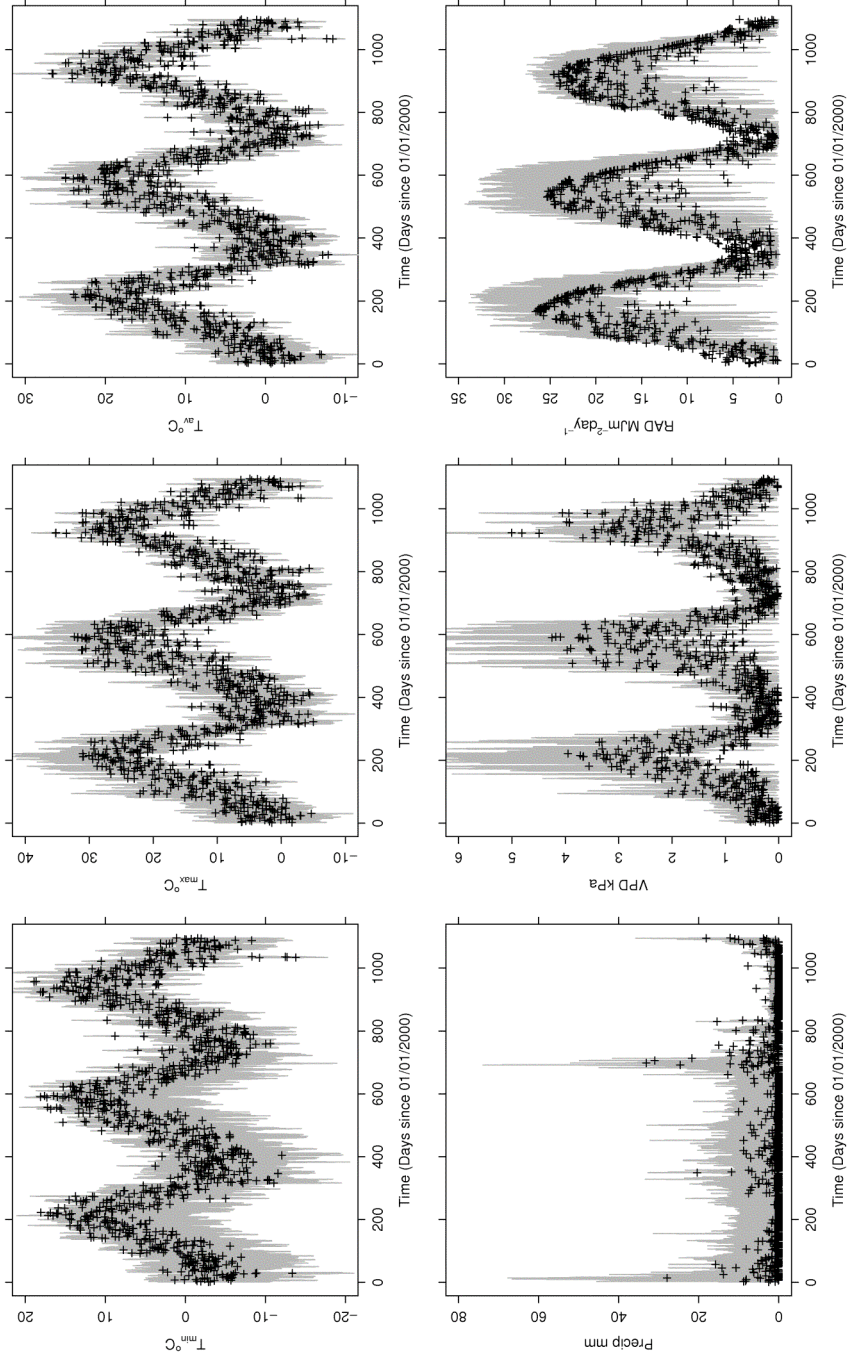


Figure 6.9 1000 meteorological time series derived from geostatistical simulation. Each element of the meteorological ensemble is indicated as a grey line, whilst observations are indicated as black crosses.

Table 6.3 Simulation versus data comparison for the Metolius Young Ponderosa pine site

Driver	Simulated		Observed		Bias	Gain	r^2
$T_{min} \text{ } ^\circ\text{C}$	2.8	(6.6)	1.3	(5.6)	0.95	0.79	0.88
$T_{max} \text{ } ^\circ\text{C}$	12.8	(9.2)	13.6	(9.8)	-0.34	1.04	0.96
$T_a \text{ } ^\circ\text{C}$	7.78	(7.7)	8.7	(7.9)	-0.88	1.01	0.97
<i>Precip mm</i> *	657.8	(273.6)	402.4	(60.9)	0.69	1.01	0.56
<i>RAD MJ m⁻² day⁻¹</i>	12.4	(7.5)	13.6	(8.5)	-0.78	1.03	0.82
<i>VPD kPa</i>	1.2	(1.0)	1.3	(1.2)	-0.04	1.13	0.91

Mean daily meteorology. Standard deviations indicated in parentheses.

*Mean annual precipitation (mm)

Table 6.4 Summary of 375 element parameter ensemble retrieved from ENKF fitting

Name	Parameter	Mean	SD	Scale
t_1	<i>Decomposition Rate</i>	3.80	(0.40)	$\times 10^{-6}$
t_2	<i>Respiration Fraction</i>	4.41	(0.22)	$\times 10^{-1}$
t_3	<i>Foliar Fraction</i>	3.30	(0.25)	$\times 10^{-1}$
t_4	<i>Root Fraction</i>	4.61	(0.19)	$\times 10^{-1}$
t_5	<i>Foliar Turnover</i>	3.64	(0.37)	$\times 10^{-3}$
t_6	<i>Woody Turnover</i>	1.90	(0.26)	$\times 10^{-4}$
t_7	<i>Root Turnover</i>	6.64	(0.58)	$\times 10^{-3}$
t_8	<i>Litter Mineralization</i>	1.63	(0.19)	$\times 10^{-2}$
t_9	<i>SOM Mineralization</i>	1.07	(0.12)	$\times 10^{-5}$
t_{10}	<i>Soil T Sensitivity</i>	6.79	(0.22)	$\times 10^{-2}$
t_{11}	<i>Photosynthetic scalar</i>	8.13	(0.39)	

and $sill_g = 32.46$ for T_{max} ; and $sill_u = 20.0$, $sill_l = 38.44$ and $sill_g = 49.3$ for precipitation (Figure 6.8). The large-scale temporal trends (Figure 6.8) operated on temporal separations greater than one month. This temporal separation was smaller than the implemented search strategy of ± 10 days, and was therefore irrelevant for the generation of simulations.

1000 simulations were drawn from the data using the specified covariance models. We generated estimates of *VPD* and *RAD* from T_{min} and T_{max} via Murray's formula ($A = 0.978$, $B = 22.23$, $C = 243.95$) and the Allen model ($K_{ra} = 0.17$), which were calibrated locally. We were able to reproduce the observed meteorology

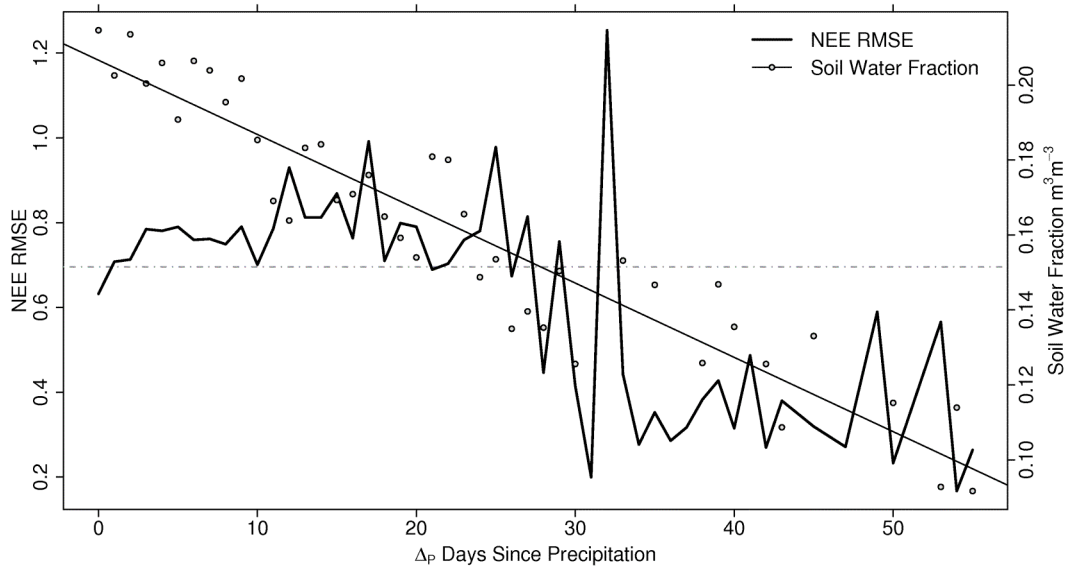


Figure 6.10 Effect of drought on NEE error. Δ_P is the number of days simulated as dry on which precipitation events were measured: Δ_P records the number of days that $P_{simulated} = 0$ whilst $P_{observed} > 0$. As Δ_P increases the model goes into mis-specified drought, as indicated by the modelled soil water fraction (right axis). The deviation in modelled and observed NEE trajectories attributable to mis-specified drought is plotted on the left axis as the root mean squared error (RMSE). The background RMSE of the model resultant from precipitation uncertainty is 0.7, indicated as a broken grey line.

successfully for all variables (Figure 6.9), with r^2 values exceeding 0.8 for all variables except P , which had an r^2 of 0.56 and a considerable positive bias (Table 6.3).

We propagated the 1000 meteorological realisations through DALEC to sample the NEE uncertainty resultant from driver uncertainty. All experiments were run using the mean parameter set retrieved from the EnKF (Table 6.4). With all meteorological observations replaced with simulated values, the model predicted a total NEE of -425 gC m^{-2} with a 95% confidence interval of $\pm 37.24 \text{ gC}$. The mean daily ensemble variance for the parameter and meteorological trajectories were 0.24 and $0.12 \text{ gC m}^{-2} \text{ day}^{-1}$ respectively, indicating significantly greater sensitivity of the model to parameterisation uncertainty ($t = 24.03$, $P < 0.0001$). Replacing only P with simulated values (experiment 2.i) resulted in a total flux of $-513 \pm 16.9 \text{ gC m}^{-2}$. Replacing all temperature (T_{min} , T_{max} , T_a) and temperature derived variables (VPD , RAD) with simulated values (experiment 2.ii)

Partitioning Sources of Model Error

resulted in a total NEE of $-338 \pm 23.66 \text{ gC m}^{-2}$. When we replaced only the temperature observations with simulated values (experiment 2.iii), a total NEE of $-337 \pm 23.66 \text{ gC m}^{-2}$ was observed (Table 6.5). Although NEE uncertainty attributable to the drivers was relatively small (typically $< 4\%$), larger differences in the total flux were observed. The directions of bias for P and temperature were opposite, but of similar magnitude ($\sim 85 \text{ gC m}^{-2}$), and seemed to cancel each other out when the full meteorological uncertainty was propagated through the model (Table 6.5), and the total NEE estimated in experiments 1 and 2 were well within one standard deviation of each other, and were not significantly different ($t = 0.37$, $P = 0.71$).

We examined the temporal period over which drought stress occurred, by comparing the number of days since the last predicted rainfall event for each simulation with the observed rainfall regime (Δ_p). Positive values of Δ_p indicated that the model was going into drought while the observed P was greater than zero (mis-specification). The maximum value of Δ_p was 55 days, whilst the mean Δ_p was -3, indicating an overall positive bias in the number of simulated rainy days. Mis-specified droughts had a mean length of 3.5 days with a standard deviation of 3.9 days. The mean number of days between rainfall events for the observations was 4.1, with a standard deviation of 6.9.

Increasing Δ_p was linearly related to a decrease in modelled soil water content ($r^2 = 0.58$, $P < 0.0001$), and a corresponding decrease in ET ($r^2 = 0.29$, $P < 0.001$). The RMS error of modelled *versus* observed NEE decreased with increasing drought stress ($r^2 = 0.46$, $P < 0.0001$). Drought was initiated after approximately 30 dry days, as indicated by the step change in Figure 6.10. The background RMSE attributable to precipitation uncertainty was 0.7. When $\Delta_p < 30$ the RMSE was approximately equal to background levels (0.71). However, as $\Delta_p > 30$ the RMSE dropped to 0.39.

Table 6.5 Total NEE estimates from various uncertainty sources.

Experiment	Source of Variation	NEE gC m ⁻²			
		2000	2001	2002	Total
1	Parameters	-120 (28)	-148 (44)	-155 (41)	-423 (109)
2	Meteorology	-115 (10)	-152 (12)	-159 (7)	-425 (19)
2.i	Precipitation	-143 (5)	-186 (7)	-183 (4)	-513 (10)
2.ii	Temperature VPD and RAD	-84 (6)	-114 (8)	-140 (6)	-338 (14)
2.iii	Temperature	-82 (7)	-101 (8)	-155 (6)	-337 (14)
3	Total	-114 (30)	-148 (44)	-147 (45)	-409 (111)

Values are in gC m⁻² per time period. Standard deviations are indicated in parentheses.

Table 6.6 Effect of increasing data scarcity on NEE uncertainty. Simulations were run using the mean parameter values from Table 6.4. Meteorological data scarcity was increased via a reduction in the proximity of conditioning data through exclusion of data below the search threshold. Simulations were conditioned on the four closest stations for each search threshold.

Search Threshold (Closest Station)	2000		2001		2002		Total	
	Mean	SD	Mean	SD	Mean	SD	Mean	SD
< 25 km	-113 (11)	-152 (12)	-158 (7)	-424 (20)	-152 (12)	-158 (7)	-424 (20)	9
> 25 km	-103 (11)	-139 (14)	-165 (14)	-408 (27)	-165 (14)	-165 (14)	-408 (27)	13
> 50 km	-123 (11)	-169 (13)	-185 (17)	-477 (28)	-185 (17)	-185 (17)	-477 (28)	11
> 75 km	-120 (12)	-165 (14)	-188 (19)	-473 (33)	-188 (19)	-188 (19)	-473 (33)	14
> 100 km	-111 (14)	-169 (19)	-191 (21)	-471 (47)	-191 (21)	-191 (21)	-471 (47)	19

Mean NEE m⁻² per time period. Standard deviations indicated in parentheses.
 *95% Confidence interval of NEE expressed as a percentage of the total flux.

6.5.3 Monte Carlo Sampling of NEE Uncertainty

We generated 1000 permutations of parameter and driver combinations at random from the pool of 375 parameter sets and 1000 driver sets (sampling with replacement) and ran the model with each in turn. These runs resulted in a total predicted NEE for 2000-2 of $-409 \pm 217.56 \text{ gC m}^{-2}$ (Table 6.5). A comparison of the daily flux estimates for the main experiments (1, 2 and 3) revealed broadly similar ensemble trajectories (Figure 6.11). However, the range of experiment 2 was asymmetrical about the mean, with a greater deviation in the positive (weaker uptake) direction. As such, the summer extremes in uptake appear to be less well replicated in experiment 2 than experiment 1. Furthermore, winter uptake appeared weaker in experiment 2 in comparison with experiment 1.

Whilst the NEE variability of experiment 1 exceeded that of experiment 2, we examined the robustness of this result by increasing the variability of the meteorological ensemble in experiment 4: We decreased the amount of conditioning data to four neighbours whilst sequentially increasing the minimum distance to an observation (Table 6.6). In all cases, the NEE uncertainty attributable to meteorological uncertainty was less than the uncertainty attributable to parameter uncertainty (9 - 19% and 51% respectively). The results of experiment 4 indicate a general increase in NEE uncertainty with increasing distance to conditioning data, although results from the 25 km threshold distance were more uncertain than the results from the >50 km threshold (Table 6.6).

A comparison of the cumulative NEE allowed an examination of the growth in uncertainty over time for the three main experiments (Table 6.5, Figure 6.12). Again, the mean ensemble trajectories appear broadly similar, with little difference in total uptake

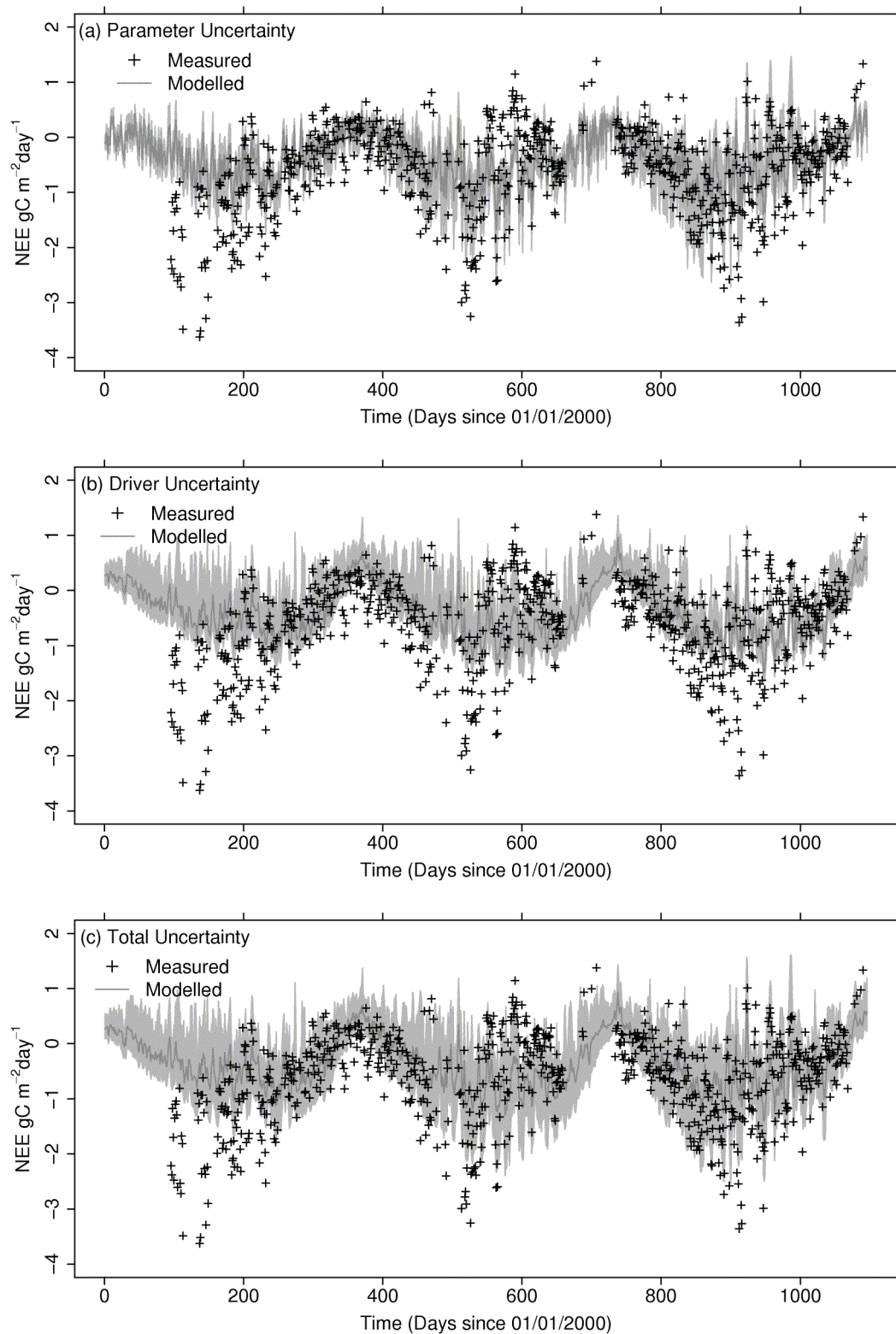


Figure 6.11 NEE trajectories for three years (2000-2002) under different uncertainty sources Ensemble ranges are indicated in light grey, whilst the ensemble mean is indicated in dark grey. Observations are represented as black crosses. Ensemble uncertainty is resultant from (a) 375 parameter sets, (b) 1000 geostatistical simulations of meteorology, (c) 1000 combinations of a and b.

Partitioning Sources of Model Error

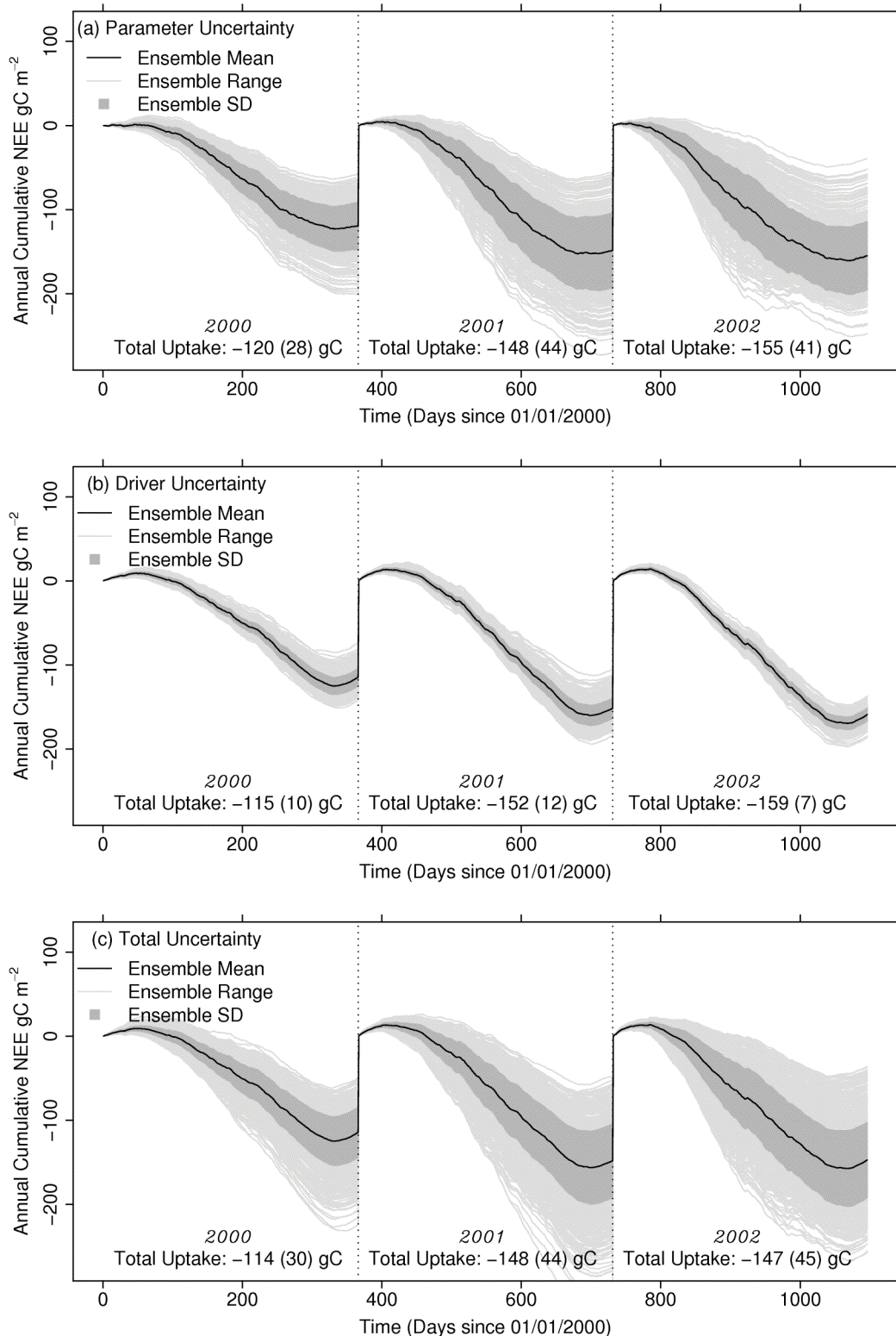


Figure 6.12 Cumulative NEE estimates over three years (2000-2002) under different sources of uncertainty. The ensemble mean is indicated in black, whilst its uncertainty is represented as a dark grey polygon. The individual ensemble members are indicated as light grey lines. Ensemble uncertainty is resultant from (a) 375 parameter sets, (b) 1000 geostatistical simulations of meteorology, (c) 1000 combinations of a and b. Mean total uptake for each year is indicated at the bottom of the plots in gC year^{-1} , with standard deviations indicated in parenthesis.

Partitioning Sources of Model Error

for inter-annual comparisons, which were approximately within one standard deviation of each other. However, it was clear that the greater variability in NEE imposed by parameter uncertainty compounds to a much larger annual uncertainty than for driver uncertainty. The total cumulative uncertainty (experiment 3, Figure 6.12c) was not very different to experiment 1, save for exaggerated extremes and a more pronounced end of season die-back, also exhibited in experiment 2 (Figure 6.12b).

6.6 Discussion

We were able to retrieve an unbiased flux estimate when parameterising DALEC using the EnKF, resulting in a total net C flux estimate consistent with the data and previous literature for the site (Law et al., 2003; Williams et al., 2005b). We found a large range of permissible parameter sets, resulting in cumulative NEE uncertainties over the three years of the study corresponding to ~50% of the total net flux (95% confidence interval of NEE expressed as a percentage of the total flux). The cumulative NEE over three years using EnKF for parameter estimation was 423 ± 90 gC m⁻² (mean \pm SD of ensemble). This mean analysis was very close to that reported by Williams et al. in an earlier study using the EnKF at the same site for state (rather than parameter) estimation, 419 ± 29 gC m² (Williams et al. 2005). The larger uncertainty associated with the parameter estimation approach was due to the constraint of setting constant parameter values for the entire 3 year run. In the state estimation approach, adjustments to the analysed C fluxes and pools were made throughout the three year period according to the observations, resulting in a closer fit to the data.

MODIS LAI retrievals compare well with ground observations (Law et al., 2003; Williams et al., 2005b) and model retrievals via data assimilation (Williams et al., 2005b).

Partitioning Sources of Model Error

However, MODIS retrievals of LAI were significantly different from the modelled LAI, and in general seem higher than we expect for the site. The fundamental issue of scale when validating 1 km² pixels against ground surveys undertaken at a scales orders of magnitude smaller makes direct comparison difficult (Tan et al., 2006; Yang et al., 2006), although published comparisons for the site report an r^2 of 76% with minimal bias (Cohen et al., 2006). Despite the large uncertainties associated with the MODIS LAI data stream, it still provides useful information due to its dense temporal coverage (8 day return period). Recent studies have indicated the use of satellite measured radiances may be preferable to LAI products in the case of assimilation, and novel ways to utilise such data streams may improve parameter constraint in the future (Quaife et al., 2008).

Meteorological simulations for the three-year period display a high degree of variability, which decreases in the final year (Figure 6.9). This decrease in uncertainty is due to observations at the nearby Metolius 'Intermediate' tower starting on project day 732 (1 January 2002). Geostatistical simulation techniques are able to reproduce the roughness of the driver fields, preserving data extremes, which may be particularly important for regionalisation of precipitation: The precipitation signal comprises of a background fluctuation ~ 0 mm, with rare but sizable events which may be on the order of 100 mm day⁻¹. Thus, reproduction of extreme events over the average behaviour may be critical, and it is in this respect that SGS confers an advantage over Kriging techniques. In general we were able to satisfactorily replicate the meteorology for the site, but issues of bias arose, particularly for precipitation.

Positive bias in precipitation simulations resulted in a positive bias in NEE estimates when all other meteorological drivers were held at their observed values. Whilst precipitation variability was comparatively large, its effects did appear to be temporally buffered by the effect of soil capacitance (Figure 6.10). A reduction in RMSE

Partitioning Sources of Model Error

error was observed with increasing drought stress that reflected a decrease in the positive bias imposed by the simulated precipitation. Drought stress manifested itself after ~ 30 days without rain. The mean length of mis-specified drought events was 3.5 days, whilst on average the simulations had an increased frequency of precipitation events with respect to the observations: On average, simulated dry spells were 3 days shorter than those measured at the site. This indicates that the time scales on which precipitation errors occur in the simulations are much shorter than the temporal scales over which drought operates in the model. Thus precipitation errors are reduced by the model, since temporal aggregation has previously been shown to reduce driver uncertainty (Spadavecchia and Williams, In review).

Despite considerable uncertainty in the simulated driver sets, the resultant NEE uncertainty was 9% of the total flux, contributing only $\sim 3\%$ to the total combined NEE uncertainty, and well within the uncertainty attributable to parameterisation. This result was robust under significant degradation of the meteorological data set, with a maximum driver uncertainty of $\sim 20\%$ when conditioning simulations on four neighbours separated by distances greater than 100 km from the study site. We therefore reject H1; that the dominant source of NEE uncertainty is due to driver uncertainty.

Experiments on the effect of data scarcity indicated a general increase in NEE uncertainty with increasing distance to conditioning data. This result is expected, given Tobler's first law of geography (Tobler, 1970), specifying that similarity of observations is directly related to separation distance. The slight increase in uncertainty of the run conditioned on data >25 km from the site over the run conditioned on data >50 km away is most likely due to the large elevation difference between the conditioning data and study site at 25 km, as this roughly corresponds to the distance between the study site and the peaks of the Cascade mountain range to the West.

Partitioning Sources of Model Error

Examining the error contribution of each driver to the NEE trajectory revealed interesting bias effects: The positive bias in simulations of precipitation elevated the estimated C uptake by $\sim 30 \text{ gC m}^{-2} \text{ year}^{-1}$, whilst smoothing of the temperature signal (overestimation of mean T_{max} underestimate of mean T_{max}) resulted in underestimation of C uptake by $\sim 30 \text{ gC m}^{-2} \text{ year}^{-1}$. These opposing signals act to cancel out when considering the total meteorological uncertainty, resulting in an unbiased estimate of total NEE, with a small uncertainty (Table 6.5).

Bias issues in the meteorological simulations are a concern, and whilst in this study the precipitation and temperature biases cancel out, it is not clear whether this was by chance alone. It is likely that the bias cancellation was fortuitous for our study site, and there may be significant bias problems for other locations and ecosystems. A broader study of these bias issues for regional meteorological drivers is thus vital.

Of the meteorological drivers considered, temperature appeared to have the largest impact on NEE uncertainty, with approximately twice the influence of precipitation on the signal. As such we reject H2a, and accept the alternative proposition that instantaneous temperature variability dominates the flux uncertainty. This is likely due to the sensitivity of both GPP and heterotrophic respiration (*via* a Q_{10} relationship) to daily air temperature in DALEC. Decoupling the effect of deriving VPD and daily insolation from temperature drivers in DALEC indicates that indirect estimation of these drivers have a minimal impact on the total NEE.

6.7 Conclusions

We were able to retrieve statistically permissible parameter sets at a data rich location, but still faced appreciable uncertainties in flux estimates resultant from

Partitioning Sources of Model Error

parameter uncertainty. As such, spatially explicit modelling exercises may struggle to characterise the regional flux without considerable fieldwork, or investment in remote sensing methodologies to retrieve well-constrained parameter sets for the region of interest. Modelling the young ponderosa pine site at Metolius is challenging, because the system is aggrading rapidly. Observed annual increases in LAI result in increasing rates of C cycling. So the model parameterisation must be able to allocate C to grow the plant tissues realistically.

Minimisation of uncertainty in regionalisations of meteorological drivers may not be critical in terms of quantification of the regional carbon budget. We found considerable variability in simulated driver trajectories resulted in a small contribution to the net uncertainty. Issues of bias in meteorological upscaling are of much greater concern, but seemed to cancel out over time when propagated through the model. It is likely that the cancellation of bias due to temperature and precipitation is by chance alone, and further research into issues of bias in driver fields is warranted.

We have presented a robust analysis of the relative magnitude of parameterisation and driver errors using novel techniques. Quantification of the uncertainty associated with regionalised meteorological fields at relevant resolutions for catchment scale studies has been presented for the first time, with significant utility for policy making, and represents a key step in the application of data assimilation approaches on the catchment scale. It appears that improved model parameterizations and calculations of bias in meteorological fields are a research priority for spatially explicit regional modeling exercises, especially where data may be sparse.

6.8 Acknowledgements

Special thanks to Bev Law, James Irvine and Meredith Kurpius for supplying flux and respiration data, and all at the Oregon Climate Service for useful advice on meteorological data sources. Thanks also to Martin De Kauwe, who supplied MODIS LAI data and provided useful remarks on the manuscript. JP Gosling also provided many useful remarks on the methodology. We would also like to thank all at the Sisters Forest Rangers Station, especially Pam Fahey who provided the vegetation classification data.

6.9 References

- Allen, R., 1997. Self-calibrating method for estimating solar radiation from air temperature. *Journal of Hydrological Engineering*, 2: 56–67.
- Ashraf, M., Loftis, J.C. and Hubbard, K.G., 1997. Application of geostatistics to evaluate partial weather station networks. *Agricultural and Forest Meteorology*, 84(3-4): 255-271.
- Canham, C.D.W., Cole, J. and Lauenroth, W.K., 2003. *Models in ecosystem science*. Princeton University Press, Princeton, N.J. ; Oxford, xv, 476 p. pp.
- Christakos, G., 1984. On the problem of permissible covariance and variogram models. *Water Resources Research*, 20(2): 251-265.
- Cohen, W.B. et al., 2006. MODIS land cover and LAI collection 4 product quality across nine sites in the western hemisphere. *IEEE Transactions on Geoscience and Remote Sensing*, 44(7): 1843-1857.
- Daly, C., Neilson, R.P. and Phillips, D.L., 1994. A statistical topographic model for mapping climatological precipitation over mountainous terrain. *Journal of Applied Meteorology*, 33(2): 140-158.
- De Cesare, L., Myers, D.E. and Posa, D., 2001. Estimating and modeling space-time correlation structures. *Statistics & Probability Letters*, 51(1): 9-14.
- De Iaco, S., Myers, D.E. and Posa, D., 2001. Space-time analysis using a general product-sum model. *Statistics & Probability Letters*, 52(1): 21-28.
- Deutsch, C.V. and Journel, A.G., 1998. *Gslib: Geostatistical software library and user's guide*. Oxford University Press, New York.
- Eknes, M. and Evensen, G., 2002. An ensemble Kalman filter with a 1-D marine ecosystem model. *Journal of Marine Science*, 36: 75-100.
- Evensen, G., 1994. Sequential data assimilation with a non-linear quasi-geostrophic model using Monte Carlo methods to forecast error statistics. *Journal of Geophysical Research*, 99: 10143-10162.
- Evensen, G., 2003. The ensemble Kalman filter: theoretical formulation and practical implementation. *Ocean Dynamics*, 53: 343-367.

- Fisher, R., Williams, M., Ruivo, M.d.L., Costa, A.L.d. and Meir, P., In press. Evaluating climatic and edaphic controls on dry season gas exchange at two Amazonian rain forest sites. *Agricultural and Forest Meteorology*.
- Fuentes, M., Kittel, T.G.F. and Nychka, D., 2006. Sensitivity of ecological models to their climate drivers: Statistical ensembles for forcing. *Ecological Applications*, 16(1): 99-116.
- Goovaerts, P., 1997. *Geostatistics for Natural Resources Evaluation*. Applied geostatistics series. Oxford University Press, New York; Oxford, xiv, 483p pp.
- Goovaerts, P., 1999. Impact of the simulation algorithm, magnitude of ergodic fluctuations and number of realizations on the spaces of uncertainty of flow properties. *Stochastic Environmental Research and Risk Assessment*, 13(3): 161-182.
- Goovaerts, P., 2000. Geostatistical approaches for incorporating elevation into the spatial interpolation of rainfall. *Journal of Hydrology*, 228(1-2): 113-129.
- Goovaerts, P., 2001. Geostatistical modelling of uncertainty in soil science. *Geoderma*, 103(1-2): 3-26.
- Gringarten, E. and Deutsch, C.V., 2001. Variogram interpretation and modeling. *Mathematical Geology*, 33(4): 507-534.
- Heuvelink, G.B.M. and Webster, R., 2001. Modelling soil variation: past, present, and future. *Geoderma*, 100(3-4): 269-301.
- Hudson, G. and Wackernagel, H., 1994. Mapping temperature using kriging with external drift - theory and an example from Scotland. *International Journal of Climatology*, 14(1): 77-91.
- Hungerford, R.D., Nemani, R.R., Running, S.W. and Coughlan, J.C., 1989. MTCLIM: a mountain microclimate simulation model. *US For. Serv. Res. Pap. INT-414*.
- Kennedy, M. et al., 2008. Quantifying uncertainty in the biospheric carbon flux for England and Wales. *Journal of the Royal Statistical Society Series a-Statistics in Society*, 171: 109-135.
- Klemedtsson, L. et al., 2007. Bayesian calibration method used to elucidate carbon turnover in forest on drained organic soil. *Biogeochemistry*, (in press). DOI 10.1007/s10533-007-9169-0.
- Knyazikhin, Y., Martonchik, J.V., Mynen, R.B., Diner, D.J. and Running, S.W., 1998. Synergistic algorithm for estimating vegetation canopy leaf area index and fraction of absorbed photosynthetically active radiation from MODIS and MISR data. *Journal of Geophysical Research*, 103(24): 32257-32276.
- Law, B.E. et al., 2001a. Carbon dioxide and water vapor exchange by young and old ponderosa pine ecosystems during a dry summer. *Tree Physiology*, 21(5): 299-308.
- Law, B.E. et al., 2001b. Spatial and temporal variation in respiration in a young ponderosa pine forests during a summer drought. *Agricultural and Forest Meteorology*, 110(1): 27-43.
- Law, B.E., Sun, O.J., Campbell, J., Van Tuyl, S. and Thornton, P.E., 2003. Changes in carbon storage and fluxes in a chronosequence of ponderosa pine. *Global Change Biology*, 9(4): 510-524.
- Law, B.E., Thornton, P.E., Irvine, J., Anthoni, P.M. and Van Tuyl, S., 2001c. Carbon storage and fluxes in ponderosa pine forests at different developmental stages. *Global Change Biology*, 7(7): 755-777.
- Law, B.E., Van Tuyl, S., Cescatti, A. and Baldocchi, D.D., 2001d. Estimation of leaf area index in open-canopy ponderosa pine forests at different successional stages and management regimes in Oregon. *Agricultural and Forest Meteorology*, 108(1): 1-14.

- Maybeck, P.S., 1979. *Stochastic Models, Estimation and Control*, 1. Academic Press, New York.
- Mcbratney, A.B. and Webster, R., 1986. Choosing functions for semi-variograms of soil properties and fitting them to sampling estimates. *Journal of Soil Science*, 37(4): 617-639.
- Murray, F.W., 1967. On the computation of saturation vapor pressure. *Journal of Applied Meteorology*, 6: 203-204.
- Myneni, R.B. et al., 2002. Global products of vegetation leaf area and fraction absorbed PAR from year one of MODIS data. *Remote Sensing of Environment*, 83: 214-231.
- Oijen, M.V., Rougier, J. and Smith, R., 2005. Bayesian calibration of process-based forest models: bridging the gap between models and data. *Tree Physiology*, 25: 915-927.
- Quaife, T. et al., 2008. Assimilating canopy reflectance data into an ecosystem model with an ensemble Kalman filter. *Remote Sensing of Environment*, 112: 1347-1364.
- Running, S.W., 1994. Testing forest-bgc ecosystem process simulations across a climatic gradient in Oregon. *Ecological Applications*, 4(2): 238-247.
- Running, S.W., Nemani, R.R. and Hungerford, R.D., 1987. Extrapolation of synoptic meteorological data in mountainous terrain and Its use for simulating forest evapotranspiration and photosynthesis. *Canadian Journal of Forest Research-Revue Canadienne De Recherche Forestiere*, 17(6): 472-483.
- Runyon, J., Waring, R.H., Goward, S.N. and Welles, J.M., 1994. Environmental Limits on Net Primary Production and Light-Use Efficiency across the Oregon Transect. *Ecological Applications*, 4(2): 226-237.
- Schwarz, P.A. et al., 2004. Climatic versus biotic constraints on carbon and water fluxes in seasonally drought-affected ponderosa pine ecosystems. *Global Biogeochemical Cycles*, 18(4): GB4007, doi:10.1029/2004GB002234,.
- Spadavecchia, L. and Williams, M., In review. Can spatio-temporal geostatistical methods improve high resolution regionalisation of meteorological variables? *Agricultural and Forest Meteorology*.
- Tan, B. et al., 2006. The impact of gridding artifacts on the local spatial properties of MODIS data: Implications for validation, compositing, and band-to-band registration across resolutions. *Remote Sensing of Environment*, 105: 98-114.
- Thiessen, A.H., 1911. Precipitation averages for large areas. *Monthly Weather Review*, 39(7): 1082-1089.
- Thornton, P.E., Running, S.W. and White, M.A., 1997. Generating surfaces of daily meteorological variables over large regions of complex terrain. *Journal of Hydrology*, 190(3-4): 214-251.
- Tobler, W.R., 1970. A computer movie simulating urban growth in the Detroit region. *Economic Geography*, 46: 234-240.
- Van Tuyl, S., Law, B.E., Turner, D.P. and Gitelman, A.I., 2005. Variability in net primary production and carbon storage in biomass across Oregon forests - an assessment integrating data from forest inventories, intensive sites, and remote sensing. *Forest Ecology and Management*, 209(3): 273-291.
- Verbeeck, H., Samson, R., Verdonck, F. and Lemeur, R., 2006. Parameter sensitivity and uncertainty of the forest carbon flux model FORUG: a Monte Carlo analysis. *Tree Physiology*, 26: 807-817.
- Wackernagel, H., 1998. *Multivariate Geostatistics: An Introduction With Applications*. Springer, Berlin; London, xiv,291p pp.

- Williams, M., Law, B.E., Anthoni, P.M. and Unsworth, M., 2001a. Use of a simulation model and ecosystem flux data to examine carbon-water interactions in ponderosa pine. *Tree Physiology*, 21: 287-298.
- Williams, M. et al., 1997. Predicting gross primary productivity in terrestrial ecosystems. *Ecological Applications*, 7(3): 882-894.
- Williams, M. et al., 2001b. Primary production of an arctic watershed: An uncertainty analysis. *Ecological Applications*, 11(6): 1800-1816.
- Williams, M., Schwarz, P., Law, B.E., Irvine, J. and Kurpius, M.R., 2005a. An improved analysis of forest carbon dynamics using data assimilation. *Global Change Biology*, 11: 89-105.
- Williams, M., Schwarz, P.A., Law, B.E., Irvine, J. and Kurpius, M.R., 2005b. An improved analysis of forest carbon dynamics using data assimilation. *Global Change Biology*, 11(1): 89-105.
- Yang, W. et al., 2006. MODIS leaf area index products: From validation to algorithm improvement. *IEEE Transactions on Geoscience and Remote Sensing*, 44(7): 1885-1898.

6.10 Appendix

In order to derive estimates of mean temperature (T_a), vapour pressure deficit (VPD) and incoming solar radiation (RAD) we implement well tested models from the literature. T_a was derived through the relationship provided in Thornton et al. (1997):

$$T_a = 0.606.T_{\max} + 0.394.T_{\min} \quad (6.2)$$

We derive VPD through a locally calibrated version of Murray's formula (Murray, 1967):

$$\begin{aligned} VPD &= e_s - e_m \\ e_s &= A.\exp\left(\frac{B.T_a}{C + T_a}\right) \\ e_m &= A.\exp\left(\frac{B.T_{\min}}{C + T_{\min}}\right) \end{aligned} \quad (6.3)$$

Where e_s is the saturation vapour pressure, e_m is the ambient vapour pressure, and A , B and C are empirical constants.

Partitioning Sources of Model Error

RAD was determined using the Allen model (Allen, 1997), which relates the atmospheric transmissivity to daily temperature range and site elevation (through atmospheric pressure):

$$\begin{aligned} RAD &= R_A \cdot K_r (T_{\max} - T_{\min})^{0.5} \\ K_r &= K_{ra} \left(\frac{P}{P_0} \right)^{0.5} \end{aligned} \tag{6.4}$$

Where R_A is the Angot (extraterrestrial) radiation in $\text{MJ m}^{-2} \text{ day}^{-1}$, P is the atmospheric pressure at the site in kPa, and P_0 is the sea level atmospheric pressure (~ 101.3 kPa). K_r is an empirical constant, which takes values ~ 0.17 for inland regions, and values of ~ 0.20 for costal regions.